

Sensitivity kernel analysis for time-domain viscoelastic full-waveform inversion based on the GSLS model

Wenyong Pan and Kris Innanen

ABSTRACT

Viscoelastic full-waveform inversion (FWI) is promising to build high-resolution subsurface velocity and quality factor Q models. Based on the generalized standard linear solid model, the attenuation effects on propagating waves can be simulated with the superposition of parallel relaxation mechanisms. However, discrepancies exist between the frameworks for constructing the sensitivity kernels in viscoelastic FWI: (I) Charara derived the sensitivity kernels for unrelaxed moduli and attenuation parameters with a perturbation approach based on Born approximation; (II) Tromp proposed to construct the Q sensitivity kernels by introducing additional adjoint source based on the Kolsky-Futterman model and frequency domain Born scattering integral; (III) Fichtner derived the sensitivity kernels for relaxation functions and Q following the adjoint-state method. The Q sensitivity kernels were constructed with the strain memory variables. This study revisits the theories of these frameworks for constructing the viscoelastic FWI sensitivity kernels. In the numerical modeling section, we calculate the sensitivity kernels within these different frameworks for comparison. Synthetic experiments are carried out to evaluate their inversion performances. We have found that the Q sensitivity kernels constructed with memory variables can resolve the Q anomalies better suffering from fewer trade-off artifacts and uncertainties in the presence of velocity errors.

INTRODUCTION

In recent decades, full-waveform inversion (FWI) methods have been intensively investigated to reconstruct high-resolution subsurface elastic properties (Tarantola, 1984; Pratt et al., 1998; Tromp et al., 2005; Virieux and Operto, 2009). However, the real Earth medium is not purely elastic. As the seismic waves propagate in subsurface, the waveforms undergo dissipation and dispersion due to attenuation (Liu et al., 1976). In viscoelastic media, the attenuation effects are commonly quantified with quality factor Q . Thus, it is attractive to build high-resolution subsurface Q profiles for describing anelastic properties of the medium using elastic FWI. The estimated Q models can be subsequently used to characterize subsurface attenuative reservoirs (Innanen, 2011) and improve seismic imaging.

Anelasticity of the Earth medium can be modelled using a phenomenological model represented mechanically by a combination of springs and dash spots. The system constructed by the parallel connection of several standard linear elements is referred to as the generalized standard linear solid (GSLS) rheology (Liu et al., 1976). In a linear viscoelastic model, the stress tensor is determined by the convolution between relaxation function and time derivative of the strain tensor (Robertsson et al., 1994). Based on the GSLS model, this convolutional constitutive relationship can be eliminated by solving a set of differential equations with the superposition of parallel relaxation mechanisms (Blanch et al., 1995). Thus, the damping effects of attenuation on propagating waves in real Earth medium can be simulated. In this study, we use the time domain spectral-element method to simulate

the wave propagation in isotropic and viscoelastic media (Komatitsch and Tromp, 2005). The sensitivity kernels (or gradients) of different physical parameters in FWI can be constructed efficiently by cross-correlating the forward and adjoint wavefields based on the adjoint-state method (Liu and Tromp, 2006). However, in time domain, the quality factor Q is not described explicitly in the rheological bodies of viscoelastic wave equation (Bohlen, 2002). Thus, it becomes problematic and complex to construct the Q sensitivity kernels. Discrepancies exist between the frameworks for constructing the sensitivity kernels in time domain viscoelastic FWI based on the GSLS model:

(I) Charara et al. (2000) derived the sensitivity kernels for the unrelaxed moduli and attenuation parameters with a perturbation approach based on Born approximation. Expressions of the sensitivity kernels for the unrelaxed moduli are the same with those in purely isotropic-elastic media. The attenuation parameters are defined as the differences between unrelaxed and relaxed modulus. The attenuation sensitivity kernels are formulated as the cross-correlation between forward strain memory variables and adjoint strain fields.

(II) Assuming that Q is constant within the seismic frequency band, (Tromp et al., 2005) derived the Q sensitivity kernels based on the Kolsky-Futterman model (Kolsky, 1952; Futterman, 1962) and frequency domain Born scattering integral. Expressions of the Q sensitivity kernels are the same with those of the corresponding moduli but with a different adjoint source. One limitation of this framework is that when simultaneously estimating velocity and Q models, different adjoint sources are needed to calculate the adjoint wavefields at each iteration, which doubles the computational cost. Furthermore, the Kolsky-Futterman model used to derive the Q sensitivity kernels is not consistent with the GSLS model in forward modelling, which may increase the inversion uncertainty. Following this approach, Pan and Innanen (2019) applied viscoelastic FWI to practical walk-away vertical seismic profile data with alternative amplitude-based misfit functions.

(III) Fichtner and van Driel (2014) derived the sensitivity kernels for relaxation functions and Q following the adjoint-state approach. The moduli sensitivity kernels can be constructed by cross-correlating the forward strain fields with the adjoint stress fields (Liu and Tromp, 2008). Whereas, the Q sensitivity kernels are calculated by cross-correlating the forward strain fields with the adjoint strain memory variables. Compared to the approach given by Tromp et al. (2005), this framework allows to calculate the velocity and Q sensitivity kernels simultaneously without introducing additional adjoint source, which reduces the computational cost a lot. Furthermore, this approach is expected to provide more accurate Q sensitivity kernels as the same physical model is used in forward modelling and sensitivity kernel derivation.

If the sensitivity kernels in viscoelastic FWI are not calculated properly, the inverted models may suffer from unexpected uncertainties more seriously. Thus, it is necessary and important to analyze the limitations and advantages of these frameworks and find the appropriate approach to construct the viscoelastic FWI sensitivity kernels. In this paper, the three frameworks described above are referred to as framework-I, -II and -III, respectively. This research revisits the theories of these frameworks for constructing the viscoelastic FWI sensitivity kernels and evaluates their performances for velocity and Q inversion. In

multiparameter FWI, the problem of interparameter trade-off complicates the inverse problem significantly (Operto et al., 2013; Innanen, 2014). In viscoelastic FWI, when using inaccurate Q models, the inverted velocity models will be distorted or damaged. Velocity errors can also produce significant trade-off artifacts in the inverted Q models (Brossier, 2011; Keating and Innanen, 2019; Pan and Innanen, 2019). Compared to the traditional waveform-difference misfit function, the envelope-difference (ED) misfit function can resolve the attenuation anomalies more effectively and naturally balance the velocity and Q updates. Thus, in this study, the sensitivity kernels are calculated within these frameworks using the ED misfit function.

In the numerical experiments, we give synthetic example with significant topographic variations and complex velocity structures. The unstructured quadrilateral mesh is created to discretize the models accounting for the topographic effects. Surface waves (SWs) are isolated from the short profiles to calculate the sensitivity kernels of S-wave velocity β and S-wave quality factor Q_β . Early arrivals of body waves (BWs) are used to calculate the sensitivity kernels of P-wave velocity α and P-wave quality factor Q_α . The influences of velocity errors on Q sensitivity kernels are evaluated for the three frameworks. The inverted velocity and Q models by inversion of SWs and BWs are also presented for comparison. In these numerical experiments, we have observed that in the presence of velocity errors, the Q sensitivity kernels calculated using the memory variables within framework-I and -III suffer from fewer trade-offs artifacts. When simultaneously inverting for velocity and Q models, these three frameworks can provide comparable quality inversion results. However, framework-II appears to converge more slowly and is almost two times more expensive than framework-I and -II.

This paper is organized as follows. The principle of forward modelling based on the GSLs model in viscoelastic media is first reviewed. We then introduce the basic theory of FWI and revisit the three different frameworks for constructing the sensitivity kernels in viscoelastic FWI. In the numerical modelling section, synthetic examples are given to analyze the sensitivity kernels within these frameworks and evaluate their performances for velocity and Q inversion.

Review of forward modelling in viscoelastic media based on the GSLs model

Wave propagation in a linear viscoelastic solid is governed by the following momentum conservation law:

$$\rho \partial_t^2 u_i - \partial_j \sigma_{ij} = f_i, \quad (1)$$

where ρ indicates mass density, f_i is the source term in the i th direction, u_i is the i th component displacement field, σ_{ij} is the stress tensor, determined by the entire history of the strain fields with the following convolutional relationship:

$$\sigma_{ij} = c_{ijkl} * \partial_t \varepsilon_{kl} = \partial_t c_{ijkl} * \varepsilon_{kl}, \quad (2)$$

where ε_{kl} is the strain tensor, the symbol “*” means time convolution, and c_{ijkl} (i, j, k, l take on the values of x, y, z) is the forth-order tensorial relaxation function:

$$c_{ijkl} = c_{ijkl}^R \left[1 + \frac{1}{P} \sum_{p=1}^P \tau_{ijkl} \mathbf{exp} \left(-\frac{t}{\tau \sigma_p} \right) \right] H, \quad (3)$$

where c_{ijkl}^R is the relaxed stiffness with $t = +\infty$ corresponding to low-frequency limit, P is the maximum number of relaxation mechanisms, H is the Heaviside function, and τ_{ijkl} describes the strength of the viscoelastic attenuation:

$$\tau_{ijkl} = \frac{\tau_{ijkl}^{\varepsilon p}}{\tau^{\sigma p}} - 1, \quad (4)$$

where $\tau_{ijkl}^{\varepsilon p}$ and $\tau^{\sigma p}$ are the strain and stress relaxation times of the p th relaxation mechanism. In isotropic and viscoelastic medium, the relaxation function is reduced to

$$c_{ijkl} = \kappa \delta_{ij} \delta_{kl} + \mu \left(\delta_{ik} \delta_{jl} + \delta_{il} \delta_{jk} - \frac{2}{3} \delta_{ij} \delta_{kl} \right), \quad (5)$$

where κ and μ are the relaxation functions of bulk and shear moduli:

$$\kappa = \kappa^R \left[1 + \frac{1}{P} \sum_{p=1}^P \tau_{\kappa} \mathbf{exp} \left(-\frac{t}{\tau^{\sigma p}} \right) \right] H, \quad (6a)$$

$$\mu = \mu^R \left[1 + \frac{1}{P} \sum_{p=1}^P \tau_{\mu} \mathbf{exp} \left(-\frac{t}{\tau^{\sigma p}} \right) \right] H, \quad (6b)$$

where κ^R and μ^R are the corresponding unrelaxed bulk and shear moduli, τ_{κ} and τ_{μ} control the strengths of the bulk modulus and shear modulus attenuation, respectively. Inserting equations (6) into equation (5) and then equation (2) gives

$$\begin{aligned} \sigma_{ij} = & \kappa^R \delta_{ij} \delta_{kl} \left[1 + \frac{1}{P} \sum_{p=1}^P \tau_{\kappa} \mathbf{exp} \left(-\frac{t}{\tau^{\sigma p}} \right) \right] H * \partial_t \varepsilon_{kl} \\ & + \mu^R \left(\delta_{ik} \delta_{jl} + \delta_{il} \delta_{jk} - \frac{2}{3} \delta_{ij} \delta_{kl} \right) \left[1 + \frac{1}{P} \sum_{p=1}^P \tau_{\mu} \mathbf{exp} \left(-\frac{t}{\tau^{\sigma p}} \right) \right] H * \partial_t \varepsilon_{kl}. \end{aligned} \quad (7)$$

The above expression is not suitable for solving initial value problem as it is required to know the whole history of the strain fields. The convolutional integral can be eliminated by taking time derivative of the stress tensor (equation (7)), yielding

$$\begin{aligned} \dot{\sigma}_{ij} = & \kappa^R \delta_{ij} \delta_{kl} \left[(\tau_{\kappa} + 1) \partial_t \varepsilon_{kl} - \sum_{p=1}^P \tau_{\kappa} \epsilon_{kl}^p \right] \\ & + \mu^R \left(\delta_{ik} \delta_{jl} + \delta_{il} \delta_{jk} - \frac{2}{3} \delta_{ij} \delta_{kl} \right) \left[(\tau_{\mu} + 1) \partial_t \varepsilon_{kl} - \sum_{p=1}^P \tau_{\mu} \epsilon_{kl}^p \right], \end{aligned} \quad (8)$$

where ϵ_{kl}^p are the strain memory variables describing the anelastic characteristics of the wavefields:

$$\epsilon_{kl}^p = \frac{1}{P \tau^{\sigma p}} \mathbf{exp} \left(-\frac{t}{\tau^{\sigma p}} \right) H * \partial_t \varepsilon_{kl}, \quad (9)$$

and time derivative of the memory variables satisfies the following first-order differential equation

$$\partial_t \epsilon_{kl}^p = -\frac{1}{\tau^{\sigma p}} \left(\epsilon_{kl}^p - \frac{1}{P} \partial_t \varepsilon_{kl} \right). \quad (10)$$

Thus, the convolution operation within the constitutive relation is replaced with a set of differential equations based on the superposition of parallel relaxation mechanisms. Combining the equations of (1), (8) and (9), wave propagation in viscoelastic medium can be simulated. The attenuation effects in viscoelastic media are always quantified with quality factor Q , which is defined in frequency domain as (Blanch et al., 1995; Bohlen, 2002)

$$\tilde{Q}^{-1}(\omega) = \frac{\mathcal{I}[\tilde{c}_{ijkl}(\omega)]}{\mathcal{R}[\tilde{c}_{ijkl}(\omega)]} = \left[\tau_{ijkl} \sum_{p=1}^P \frac{\omega\tau^{\sigma p}}{1 + (\omega\tau^{\sigma p})^2} \right] \left[P + \tau_{ijkl} \sum_{p=1}^P \frac{(\omega\tau^{\sigma p})^2}{1 + (\omega\tau^{\sigma p})^2} \right]^{-1}, \quad (11)$$

where \tilde{c}_{ijkl} indicates Fourier transform of the time derivative of the relaxation function, ω denotes angular frequency, \mathcal{R} and \mathcal{I} mean real and imaginary parts, respectively. To approximate a nearly constant value of Q_{ref}^{-1} within the seismic frequency band, the parameters of relaxation times τ_{ijkl} and $\tau^{\sigma p}$ can be obtained by minimizing the distance between Q_{ref}^{-1} and equation (11) through a least-squares nonlinear optimization process (Bohlen, 2002). In this study, I use a number of 3 relaxation mechanisms to approximate constant Q in the forward modelling experiments.

Sensitivity kernels for viscoelastic FWI

Sensitivity kernels in FWI measure the sensitivities of misfit function with respect to the model parameters and thus are essentially important to update the model parameters effectively. With the adjoint-state approach, the sensitivity kernels can be constructed efficiently by cross-correlating the forward and adjoint wavefields without calculating the Fréchet derivative wavefield explicitly. Quality factor Q is commonly used to quantify the attenuation effects in linear viscoelastic solid. It is attractive to build high-resolution subsurface Q models using viscoelastic FWI. However, Q is not explicitly described in the rheological bodies, as introduced in the forward modelling section. Thus, it is problematic to construct the Q sensitivity kernels.

Researchers have developed different frameworks to construct the viscoelastic FWI sensitivity kernels based on the GSLs model in time domain. However, the sensitivity kernels within these frameworks are given with different formulas. If the sensitivity kernels are not calculated properly, the inverted models may suffer from unexpected uncertainties. Currently, few researchers investigate their mechanisms and evaluate the inversion performances. In the following sections, we revisit the theories of the main three frameworks for calculating the sensitivity kernels in time domain viscoelastic FWI based on the GSLs model.

Framework-I

Charara et al. (2000) derived the sensitivity kernels for moduli and attenuation parameters with a perturbation approach based on Born approximation. At time $t = 0^+$, the relaxation function in equation (3) reduces to the unrelaxed stiffness tensor corresponding

to high-frequency limit:

$$c_{ijkl}^U = c_{ijkl}^R \left[1 + \frac{1}{P} \sum_{p=1}^P \tau_{ijkl} \right] = c_{ijkl}^R (1 + \tau_{ijkl}). \quad (12)$$

The difference between the relaxed and unrelaxed stiffness tensor is given by

$$\delta c_{ijkl} = c_{ijkl}^R - c_{ijkl}^U = -\tau_{ijkl} c_{ijkl}^R = -\frac{\tau_{ijkl}}{(1 + \tau_{ijkl})} c_{ijkl}^U. \quad (13)$$

The stiffness difference δc_{ijkl} is proportional to τ_{ijkl} and thus measures the attenuation magnitude. The relaxation function can be expressed in terms of c_{ijkl}^U and δc_{ijkl} :

$$c_{ijkl} = (c_{ijkl}^U + \delta c_{ijkl}) \left[1 + \frac{1}{P} \sum_{p=1}^P \tau_{ijkl} \mathbf{exp} \left(-\frac{t}{\tau^{\sigma p}} \right) \right] H, \quad (14)$$

Within the seismic frequency band, the ratio of c_{ijkl}^U to c_{ijkl}^R can be assumed to be constant (Charara et al., 2000):

$$\frac{c_{ijkl}^U}{c_{ijkl}^R} = \frac{\tau_{ijkl}^{\varepsilon p}}{\tau^{\sigma p}} = \text{constant}. \quad (15)$$

Thus, time derivative of the relaxation function can be derived as

$$\partial_t c_{ijkl} = c_{ijkl}^U + \delta c_{ijkl} \left[\frac{1}{P} \sum_{p=1}^P \frac{1}{\tau^{\sigma p}} \mathbf{exp} \left(-\frac{t}{\tau^{\sigma p}} \right) \right] H, \quad (16)$$

Inserting equation (16) into equation (2) yields

$$\sigma_{ij} = c_{ijkl}^U \varepsilon_{kl} + \delta c_{ijkl} \sum_{p=1}^P \hat{\varepsilon}_{kl}^p, \quad (17)$$

where $\hat{\varepsilon}_{kl}^p$ are the strain memory variables

$$\hat{\varepsilon}_{kl}^p = \frac{1}{P \tau^{\sigma p}} \mathbf{exp} \left(-\frac{t}{\tau^{\sigma p}} \right) H * \varepsilon_{kl}. \quad (18)$$

Note that the strain memory variables $\hat{\varepsilon}_{kl}^p$ in equation (18) are slightly different from the strain memory variables ε_{kl}^p in equation (9). Considering that a viscoelastic anomaly is embedded in an infinite homogeneous background with the properties of ρ , c_{ijkl}^U and δc_{ijkl} , the differences between the perturbed and unperturbed model properties are defined as

$$\Delta \rho = \check{\rho} - \rho, \Delta c_{ijkl}^U = \check{c}_{ijkl}^U - c_{ijkl}^U, \Delta \delta c_{ijkl} = \delta \check{c}_{ijkl} - \delta c_{ijkl}, \quad (19)$$

where $\check{\rho}$, \check{c}_{ijkl}^U and $\delta \check{c}_{ijkl}$ indicate the model parameters of the perturbed inclusion, $\Delta \rho$, Δc_{ijkl}^U and $\Delta \delta c_{ijkl}$ indicate the corresponding model perturbations. Assuming that the size of the inclusion is much smaller than the wavelength of the incident wave, the perturbed wavefield due to these model perturbations can be written as

$$\Delta \mathbf{u} = \check{\mathbf{u}} - \mathbf{u}, \quad (20)$$

where $\check{\mathbf{u}}$ indicate the perturbed displacement wavefield. Inserting equations (19) and (20) into the equation of motion gives:

$$(\rho + \Delta\rho) \partial_t^2 (u_i + \Delta u_i) - \partial_j (\sigma_{ij} + \Delta\sigma_{ij}) = f_i,$$

$$\sigma_{ij} + \Delta\sigma_{ij} = (c_{ijkl}^U + \Delta c_{ijkl}^U) (\varepsilon_{kl} + \Delta\varepsilon_{kl}) + (\Delta c_{ijkl} + \Delta\delta c_{ijkl}) \sum_{p=1}^P (\hat{\varepsilon}_{kl}^p + \Delta\hat{\varepsilon}_{kl}^p). \quad (21)$$

Neglecting the high-order terms in equation (21) based on Born approximation, the equation of motion splits into the following two equations:

$$\rho \partial_t^2 u_i - \partial_j \sigma_{ij} = f_i, \quad (22a)$$

$$\rho \partial_t^2 \Delta u_i - \partial_j \left(c_{ijkl}^R \Delta\varepsilon_{kl} + \delta c_{ijkl} \sum_{p=1}^P \Delta\hat{\varepsilon}_{kl}^p \right) = \partial_j \Delta M_{ij} - \Delta\rho \partial_t^2 u_i, \quad (22b)$$

where ΔM_{ij} indicates the equivalent moment tensor source:

$$\Delta M_{ij} = \Delta c_{ijkl}^R \varepsilon_{kl} + \Delta\delta c_{ijkl} \sum_{p=1}^P \hat{\varepsilon}_{kl}^p. \quad (23)$$

Equation (22)a describes the propagation of incident wave in the homogeneous background medium, whereas equation (22)b describes the propagation of scattered wave. The interaction of incident wave with the model perturbations on the right side of equation (22)b serves as the virtual scattering source. Solving equation (22)b and applying integration by parts with far-field approximation, the wavefield perturbation can be expressed in terms of Green's functions with representation theorem:

$$\Delta u_n = - \int_{\Omega} \int_0^{t'} \left(\Delta\rho G_{ni} \partial_t^2 u_i + \Delta c_{ijkl}^U \partial_j G_{ni} \varepsilon_{kl} + \Delta\delta c_{ijkl} \partial_j G_{ni} \sum_{p=1}^P \hat{\varepsilon}_{kl}^p \right) dt' d\mathbf{x} \quad (24)$$

In isotropic and viscoelastic media, the wavefield perturbation due to the perturbations $\Delta\rho$, $\Delta\kappa^U$, $\Delta\mu^U$, $\Delta\delta\kappa$ and $\Delta\delta\mu$ for the model parameters of ρ , unrelaxed bulk modulus κ^U , unrelaxed shear modulus μ^U , moduli differences of $\delta\kappa = \kappa^R - \kappa^U$ and $\delta\mu = \mu^R - \mu^U$ is obtained as

$$\begin{aligned} \Delta u_n = & - \int_{\Omega} \int_0^{t'} \Delta\rho G_{ni} \partial_t^2 u_i dt d\mathbf{x} \\ & - \int_{\Omega} \int_0^{t'} \Delta\kappa^U \delta_{ij} \delta_{kl} \partial_j G_{ni} \varepsilon_{kl} dt d\mathbf{x} \\ & - \int_{\Omega} \int_0^{t'} \Delta\mu^U \left(\delta_{ik} \delta_{jl} + \delta_{jk} \delta_{il} - \frac{2}{3} \delta_{ij} \delta_{kl} \right) \partial_j G_{ni} \varepsilon_{kl} dt d\mathbf{x} \\ & - \int_{\Omega} \int_0^{t'} \Delta\delta\kappa \delta_{ij} \delta_{kl} \partial_j G_{ni} \sum_{p=1}^P \hat{\varepsilon}_{kl}^p dt d\mathbf{x} \\ & - \int_{\Omega} \int_0^{t'} \Delta\delta\mu \left(\delta_{ik} \delta_{jl} + \delta_{jk} \delta_{il} - \frac{2}{3} \delta_{ij} \delta_{kl} \right) \partial_j G_{ni} \sum_{p=1}^P \hat{\varepsilon}_{kl}^p dt d\mathbf{x}. \end{aligned} \quad (25)$$

The sensitivity kernels for ρ , κ^U , μ^U , $\delta\kappa$ and $\delta\mu$ within framework-I are given by:

$$K_{\rho}^I = - \int_0^{t'} \rho u_i^{\dagger} \partial_t^2 u_i dt, \quad (26a)$$

$$K_{\kappa^U}^I = - \int_0^{t'} \kappa^U \delta_{ij} \delta_{kl} \varepsilon_{ij}^{\dagger} \varepsilon_{kl} dt, \quad (26b)$$

$$K_{\mu^U}^I = - \int_0^{t'} \mu^U \left(\delta_{ik} \delta_{jl} + \delta_{jk} \delta_{il} - \frac{2}{3} \delta_{ij} \delta_{kl} \right) \varepsilon_{ij}^{\dagger} \varepsilon_{kl} dt, \quad (26c)$$

$$K_{\delta\kappa}^I = - \int_0^{t'} \delta\kappa \delta_{ij} \delta_{kl} \varepsilon_{ij}^{\dagger} \sum_{p=1}^P \hat{\varepsilon}_{kl}^p dt, \quad (26d)$$

$$K_{\delta\mu}^I = - \int_0^{t'} \delta\mu \left(\delta_{ik} \delta_{jl} + \delta_{jk} \delta_{il} - \frac{2}{3} \delta_{ij} \delta_{kl} \right) \varepsilon_{ij}^{\dagger} \sum_{p=1}^P \hat{\varepsilon}_{kl}^p dt, \quad (26e)$$

where u_i^{\dagger} is the adjoint displacement field:

$$u_i^{\dagger} = G_{in} * f_n^{\dagger}, \quad (27)$$

where f_n^{\dagger} is the adjoint source of the WD misfit function:

$$f_n^{\dagger} = u_n - d_n. \quad (28)$$

The expressions of the unrelaxed moduli sensitivity kernels $K_{\kappa^U}^I$ and $K_{\mu^U}^I$ are the same with the moduli sensitivity kernels in purely isotropic-elastic media. The attenuation sensitivity kernels $K_{\delta\kappa}^I$ and $K_{\delta\mu}^I$ can be constructed by cross-correlating the forward strain memory variables and adjoint strain fields.

Framework-II

In this section, we follow the approach given by Tromp et al. (2005) to derive the Q sensitivity kernels. With the assumption of that Q is constant over a wide range of seismic frequencies, the moduli can be expressed in terms of the quality factors in frequency domain by

$$\tilde{\kappa}(\omega) = \tilde{\kappa}(\omega_0) \left[1 + \frac{2}{\pi \tilde{Q}_{\kappa}} \ln \frac{|\omega|}{\omega_0} - i \operatorname{sgn}(\omega) \frac{1}{\tilde{Q}_{\kappa}} \right], \quad (29a)$$

$$\tilde{\mu}(\omega) = \tilde{\mu}(\omega_0) \left[1 + \frac{2}{\pi \tilde{Q}_{\mu}} \ln \frac{|\omega|}{\omega_0} - i \operatorname{sgn}(\omega) \frac{1}{\tilde{Q}_{\mu}} \right], \quad (29b)$$

where $\tilde{\kappa}$ and $\tilde{\mu}$ are the bulk and shear moduli in frequency domain, \tilde{Q}_{κ} and \tilde{Q}_{μ} are the corresponding frequency domain quality factors, "ln" means natural logarithm, ω_0 is the reference angular frequency, i denotes imaginary unit, and $\operatorname{sgn}(\omega)$ indicates the sign of ω . Variations of $\tilde{\kappa}$ and $\tilde{\mu}$ due to the perturbations of \tilde{Q}_{κ} and \tilde{Q}_{μ} are given by

$$\Delta \tilde{\kappa}(\omega) = \frac{\tilde{\kappa}(\omega_0)}{\tilde{Q}_{\kappa}^2} \left[-\frac{2}{\pi} \ln \frac{|\omega|}{\omega_0} + i \operatorname{sgn}(\omega) \right] \Delta \tilde{Q}_{\kappa}, \quad (30a)$$

$$\Delta \tilde{\mu}(\omega) = \frac{\tilde{\mu}(\omega_0)}{\tilde{Q}_{\mu}^2} \left[-\frac{2}{\pi} \ln \frac{|\omega|}{\omega_0} + i \operatorname{sgn}(\omega) \right] \Delta \tilde{Q}_{\mu}. \quad (30b)$$

Thus, following the chain rule and using the frequency domain version of Born approximation, the Q sensitivity kernels can be expressed with the corresponding moduli sensitivity kernels in time domain:

$$K_{Q_\kappa}^{II} = -\frac{K_\kappa^{Q_\kappa}}{Q_\kappa}, K_{Q_\mu}^{II} = -\frac{K_\mu^{Q_\mu}}{Q_\mu}, \quad (31)$$

where the expressions of $K_\kappa^{Q_\kappa}$ and $K_\mu^{Q_\mu}$ are the same with those of $K_{\kappa U}^I$ and $K_{\mu U}^I$ in framework-I (see equation (26)) but with a different adjoint source $f_{i,Q}^\dagger$ (Tromp et al., 2005):

$$f_{i,Q}^\dagger(t) = \frac{1}{2\pi} \int_{-\infty}^{+\infty} \left[\frac{2}{\pi} \ln \frac{|\omega|}{\omega_0} - i \operatorname{sgn}(\omega) \right] \tilde{f}_i^\dagger(\omega) \mathbf{exp}(i\omega t) d\omega, \quad (32)$$

where \tilde{f}_i^\dagger is the regular adjoint source of the WD misfit function (equation (28)) in frequency domain. The first term in the adjoint source $f_{i,Q}^\dagger$ involving $\ln(|\omega|/\omega_0)$ controls physical dispersion of the seismic signals, whereas the second term is simply the Hilbert transform of the regular adjoint source \tilde{f}_i^\dagger measuring the amplitude variations of the seismic data (Tromp et al., 2005). Within this framework, the moduli sensitivity kernels K_κ^{II} and K_μ^{II} are the same with those in purely isotropic-elastic media. Herein, we use the moduli sensitivity kernels $K_{\kappa U}^I$ and $K_{\mu U}^I$ in framework-I instead.

Framework-III

Following Fichtner and van Driel (2014), the quality factors Q_κ and Q_μ can be incorporated into the constitutive relation with the enforcements of $\tau_\kappa = Q_\kappa^{-1}$ and $\tau_\mu = Q_\mu^{-1}$, yielding

$$\begin{aligned} \sigma_{ij} = & \kappa^R \delta_{ij} \delta_{kl} \left[1 + \frac{1}{P} \sum_{p=1}^P \frac{1}{Q_\kappa} \mathbf{exp} \left(-\frac{t}{\tau^{\sigma p}} \right) \right] H * \partial_t \varepsilon_{kl} \\ & + \mu^R \left(\delta_{ik} \delta_{jl} + \delta_{il} \delta_{jk} - \frac{2}{3} \delta_{ij} \delta_{kl} \right) \left[1 + \frac{1}{P} \sum_{p=1}^P \frac{1}{Q_\mu} \mathbf{exp} \left(-\frac{t}{\tau^{\sigma p}} \right) \right] H * \partial_t \varepsilon_{kl}. \end{aligned} \quad (33)$$

Thus, the Q sensitivity kernels in viscoelastic FWI can be directly derived following the standard adjoint-state approach by inserting the above constitutive relation into the equation of motion. The Lagrangian formulation of the WD misfit function is given by (Liu and Tromp, 2006, 2008; Fichtner and van Driel, 2014)

$$\begin{aligned} \hat{\chi}(\mathbf{m}) = & \frac{1}{2} \sum_{\mathbf{x}_r} \int_0^{t'} [u_i(\mathbf{m}) - d_i]^2 dt \\ & - \int_0^{t'} \int_\Omega \lambda_i [\rho \partial_t^2 u_i - f_i - \partial_j (\kappa \delta_{ij} \delta_{kl} * \partial_t \varepsilon_{kl})] d\mathbf{x} dt \\ & + \int_0^{t'} \int_\Omega \lambda_i \partial_j \left[\mu \left(\delta_{ik} \delta_{jl} + \delta_{il} \delta_{jk} - \frac{2}{3} \delta_{ij} \delta_{kl} \right) * \partial_t \varepsilon_{kl} \right] d\mathbf{x} dt. \end{aligned} \quad (34)$$

Following the adjoint-state method, variation of the Lagrangian misfit function due to the perturbations of the model parameters ρ , κ , μ , Q_κ and Q_μ can be derived as

$$\begin{aligned}
\Delta \hat{\chi} = & \int_0^{t'} \int_{\Omega} \sum_{\mathbf{x}_r} [u_i - d_i] \Delta u_i d\mathbf{x} dt \\
& - \int_0^{t'} \int_{\Omega} [\rho \partial_t^2 \lambda_i - \partial_j (\kappa \delta_{ij} \delta_{kl} * \partial_t \tilde{\epsilon}_{kl})] \Delta u_i d\mathbf{x} dt \\
& + \int_0^{t'} \int_{\Omega} \partial_j \left[\mu \left(\delta_{ik} \delta_{jl} + \delta_{il} \delta_{jk} - \frac{2}{3} \delta_{ij} \delta_{kl} \right) * \partial_t \tilde{\epsilon}_{kl} \right] \Delta u_i d\mathbf{x} dt \\
& - \int_0^{t'} \int_{\Omega} \Delta \rho \lambda_i \partial_t^2 u_i d\mathbf{x} dt \\
& - \int_0^{t'} \int_{\Omega} (\Delta \kappa * \partial_t \tilde{\epsilon}_{ii}) \epsilon_{kk} d\mathbf{x} dt \\
& - \int_0^{t'} \int_{\Omega} \left[\Delta \mu \left(\delta_{ik} \delta_{jl} + \delta_{il} \delta_{jk} - \frac{2}{3} \delta_{ij} \delta_{kl} \right) * \partial_t \tilde{\epsilon}_{ij} \right] \epsilon_{kl} d\mathbf{x} dt \\
& + \int_0^{t'} \int_{\Omega} \left(\Delta Q_\kappa \frac{\kappa^R}{Q_\kappa^2} \sum_{p=1}^P \tau^{\sigma p} \tilde{\epsilon}_{ii}^p \right) \epsilon_{kk} d\mathbf{x} dt \\
& + \int_0^{t'} \int_{\Omega} \left[\Delta Q_\mu \frac{\mu^R}{Q_\mu^2} \left(\delta_{ik} \delta_{jl} + \delta_{il} \delta_{jk} - \frac{2}{3} \delta_{ij} \delta_{kl} \right) \sum_{p=1}^P \tau^{\sigma p} \tilde{\epsilon}_{ij}^p \right] \epsilon_{kl} d\mathbf{x} dt,
\end{aligned} \tag{35}$$

where $\tilde{\epsilon}_{ij} = \partial_j \lambda_i$ is the Lagrangian strain field, and $\tilde{\epsilon}_{ij}^p$ are the Lagrangian strain memory variables:

$$\tilde{\epsilon}_{ij}^p = \frac{1}{P \tau^{\sigma p}} \mathbf{exp} \left(-\frac{t}{\tau^{\sigma p}} \right) H * \partial_t \tilde{\epsilon}_{ij}. \tag{36}$$

The Lagrangian is stationary with respect to Δu_i in the absence of the perturbations $\Delta \rho$, $\Delta \kappa$, $\Delta \mu$, ΔQ_κ and ΔQ_μ (Liu and Tromp, 2006). Thus, the adjoint-state equation can be obtained by setting the coefficient of Δu_i as zero:

$$\rho \partial_t^2 \lambda_i - \partial_j \left[\kappa \delta_{ij} \delta_{kl} * \partial_t \tilde{\epsilon}_{kl} + \mu \left(\delta_{ik} \delta_{jl} + \delta_{il} \delta_{jk} - \frac{2}{3} \delta_{ij} \delta_{kl} \right) * \partial_t \tilde{\epsilon}_{kl} \right] = -(d_i - u_i), \tag{37}$$

Thus, gradient of Lagrangian misfit function can be obtained as

$$\nabla_{\mathbf{m}} \hat{\chi} = - \left(\frac{K_\rho^{III}}{\rho} + \frac{K_\kappa^{III}}{\kappa} + \frac{K_\mu^{III}}{\mu} + \frac{K_{Q_\kappa}^{III}}{Q_\kappa} + \frac{K_{Q_\mu}^{III}}{Q_\mu} \right), \tag{38}$$

where K_ρ^{III} , K_κ^{III} , K_μ^{III} , $K_{Q_\kappa}^{III}$ and $K_{Q_\mu}^{III}$ are the corresponding sensitivity kernels for ρ , κ , μ , Q_κ and Q_μ models in framework-III. Their explicit expressions are listed in the follow-

ing:

$$K_{\rho}^{III} = - \int_0^{t'} \rho u_i^{\dagger} \partial_t^2 u_i dt, \quad (39a)$$

$$K_{\kappa}^{III} = - \int_0^{t'} \left(\kappa * \partial_t \varepsilon_{ii}^{\dagger} \right) \varepsilon_{kk} dt, \quad (39b)$$

$$K_{\mu}^{III} = - \int_0^{t'} \left[\mu \left(\delta_{ik} \delta_{jl} + \delta_{il} \delta_{jk} - \frac{2}{3} \delta_{ij} \delta_{kl} \right) * \partial_t \varepsilon_{ij}^{\dagger} \right] \varepsilon_{kl} dt, \quad (39c)$$

$$K_{Q_{\kappa}}^{III} = \int_0^{t'} \left(\frac{\kappa^R}{Q_{\kappa}} \sum_{p=1}^P \tau^{\sigma p} \varepsilon_{ii}^{p,\dagger} \right) \varepsilon_{kk} dt, \quad (39d)$$

$$K_{Q_{\mu}}^{III} = \int_0^{t'} \left[\frac{\mu^R}{Q_{\mu}} \left(\delta_{ik} \delta_{jl} + \delta_{il} \delta_{jk} - \frac{2}{3} \delta_{ij} \delta_{kl} \right) \sum_{p=1}^P \tau^{\sigma p} \varepsilon_{ij}^{p,\dagger} \right] \varepsilon_{kl} dt, \quad (39e)$$

where u_i^{\dagger} is the adjoint displacement field defined as the time-reversed Lagrangian field, $\varepsilon_{ij}^{\dagger}$ and $\varepsilon_{ij}^{p,\dagger}$ are the adjoint strain fields and adjoint strain memory variables.

Velocity- Q model parameterization

In the above section, the sensitivity kernels of moduli and attenuation parameters are given in different frameworks. However, in practical FWI experiments, the viscoelastic media is commonly parameterized with density ρ' , P-wave velocity α , S-wave velocity β , P-wave quality factor Q_{α} and S-wave quality factor Q_{β} , which is referred to as the velocity- Q model parameterization. In this section, we derive the sensitivity kernels in velocity- Q model parameterization for viscoelastic FWI.

In framework-I, Charara et al. (2000) derived the sensitivity kernels for ρ , κ^U , μ^U , $\delta\kappa$ and $\delta\mu$. Herein, with the enforcement of $\tau_{\kappa} = Q_{\kappa}^{-1}$ and $\tau_{\mu} = Q_{\mu}^{-1}$ given by Fichtner and van Driel (2014), the attenuation parameters $\delta\kappa$ and $\delta\mu$ are related to the moduli quality factors Q_{κ} and Q_{μ} by

$$\begin{aligned} \delta\kappa &= - \frac{\tau_{\kappa}}{1 + \tau_{\kappa}} \kappa^U = - \frac{1}{1 + Q_{\kappa}} \kappa^U, \\ \delta\mu &= - \frac{\tau_{\mu}}{1 + \tau_{\mu}} \mu^U = - \frac{1}{1 + Q_{\mu}} \mu^U, \end{aligned} \quad (40)$$

Thus, following the chain rule, the sensitivity kernels for Q_{κ} and Q_{μ} within framework-I can be obtained as

$$K_{Q_{\kappa}}^I = - \frac{Q_{\kappa}}{1 + Q_{\kappa}} K_{\delta\kappa}^I, K_{Q_{\mu}}^I = - \frac{Q_{\mu}}{1 + Q_{\mu}} K_{\delta\mu}^I. \quad (41)$$

According to Dahlen & Tromp (1998), the velocity quality factors Q_{α} and Q_{β} can be expressed with the modulus quality factors Q_{κ} and Q_{μ} by

$$Q_{\kappa} = \frac{\alpha^2 - \beta^2}{\alpha^2 Q_{\alpha}^{-1} - \beta^2 Q_{\beta}^{-1}}, Q_{\mu} = Q_{\beta}. \quad (42)$$

Thus, following the chain rule, the sensitivity kernels for ρ' , α , β , Q_α and Q_β models in velocity- Q model parameterization can be expressed in terms of the sensitivity kernels in modulus- Q parameterization by (Pan and Innanen, 2019)

$$K_{\rho'} = K_\rho + K_\kappa + K_\mu, \quad (43a)$$

$$K_\alpha = \frac{6\alpha^2}{3\alpha^2 - 4\beta^2} K_\kappa + \left(\frac{2\alpha^2}{\alpha^2 - \beta^2} - \frac{2\alpha^2 Q_\beta}{\alpha^2 Q_\beta - \beta^2 Q_\alpha} \right) K_{Q_\kappa}, \quad (43b)$$

$$K_\beta = 2 \left(K_\mu - \frac{4\beta^2}{3\alpha^2 - 4\beta^2} K_\kappa \right) + \left(\frac{2\beta^2 Q_\alpha}{\alpha^2 Q_\beta - \beta^2 Q_\alpha} - \frac{2\beta^2}{\alpha^2 - \beta^2} \right) K_{Q_\kappa}, \quad (43c)$$

$$K_{Q_\alpha} = \frac{\alpha^2 Q_\beta}{Q_\beta \alpha^2 - \beta^2 Q_\alpha} K_{Q_\kappa}, \quad (43d)$$

$$K_{Q_\beta} = K_{Q_\mu} - \frac{\beta^2 Q_\alpha}{\alpha^2 Q_\beta - \beta^2 Q_\alpha} K_{Q_\kappa}. \quad (43e)$$

The relationships in equation (43) work for all of the three frameworks. Thus, in the inversion process, the velocity and Q models can be updated and estimated.

Envelope-difference misfit function

The envelope misfit function is commonly used to reduce the cycle-skipping difficulty in FWI. Compared to the traditional WD misfit function, the envelope-difference (ED) misfit function shows stronger sensitivity to Q anomaly and can naturally balance the velocity and Q updates. In this study, the ED misfit function is used to calculate the velocity and Q sensitivity kernels in viscoelastic FWI:

$$\chi^{\text{ED}}(\mathbf{m}) = \frac{1}{2} \sum_{\mathbf{x}_r} \int_0^{t'} [E_i(\mathbf{m}) - E_i^{\text{obs}}]^2 dt, \quad (44)$$

where E_i^{obs} and E_i represent the envelope of observed and synthetic data, respectively. Variation of the ED misfit function due to the perturbations of the model parameters is obtained as

$$\Delta \chi^{\text{ED}} = \sum_{\mathbf{x}_r} \int_0^{t'} \frac{E_i - E_i^{\text{obs}}}{E_i} u_i \Delta u_i - \mathcal{H} \left[\frac{E_i - E_i^{\text{obs}}}{E_i} \mathcal{H}(u_i) \right] \Delta u_i dt, \quad (45)$$

where \mathcal{H} means Hilbert transform. The adjoint source of the ED misfit function is obtained as

$$f_{i,\text{ED}}^\dagger = \frac{E_i - E_i^{\text{obs}}}{E_i} u_i - \mathcal{H} \left[\frac{E_i - E_i^{\text{obs}}}{E_i} \mathcal{H}(u_i) \right]. \quad (46)$$

When using the ED misfit function, the sensitivity kernels in viscoelastic FWI can be constructed with the adjoint source $f_{i,\text{ED}}^\dagger$ without changing their expressions.

NUMERICAL EXPERIMENTS

Canadian Foothill model example with irregular topography

In Figures 1a-1d, we present the true α , β , Q_α and Q_β models with irregular topography. The topography surface is indicated by the black lines. The white area indicates the air

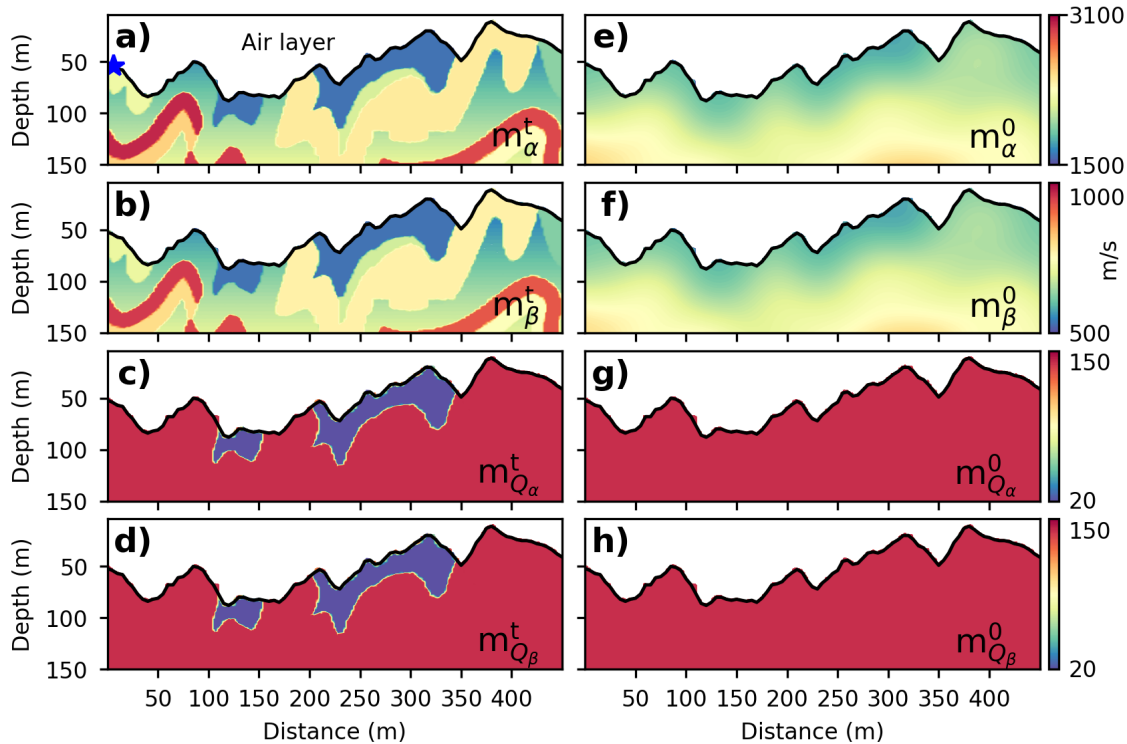


FIG. 1. (a-d) are the true α , β , Q_α and Q_β models (\mathbf{m}_α^t , \mathbf{m}_β^t , $\mathbf{m}_{Q_\alpha}^t$ and $\mathbf{m}_{Q_\beta}^t$); (f-j) are the corresponding initial models (\mathbf{m}_α^0 , \mathbf{m}_β^0 , $\mathbf{m}_{Q_\alpha}^0$ and $\mathbf{m}_{Q_\beta}^0$). The blue star in (a) indicates the source located at (0 m, 2 m). This figure is adapted from Figure 10 in Pan et al. (2020).

layer. We create the true β model from the true α model with $\alpha/\beta = 3$. Because the unconsolidated formations at near-surface always show strong attenuation and low velocity, the true Q_α and Q_β models are created by embedding two strong Q anomalies ($Q_\alpha = Q_\beta = 20$) in the homogeneous background ($Q_\alpha = Q_\beta = 150$) overlapped with the low velocity zones, as shown in Figures 1c-1d. The initial α and β models are created by smoothing the corresponding true models, as presented in Figures 1e-1f. Figures 1g-1h are the initial Q_α and Q_β models with a constant value of 150. In the numerical experiments, we ignore the influence of density. The true and initial density models are homogeneous with a constant value of 1800 kg/m^3 . The model is 450 m wide in horizontal direction. The maximum depth from the topography surface to the bottom is 150 m. To account for the topographic effects, unstructured quadrilateral mesh grid with 30 and 90 elements in vertical and horizontal directions are generated to discretize the models. Free-surface boundary condition is applied on the topographic surface and absorbing boundary condition is applied on the other sides of the model. A number of 33 sources and 151 receivers are distributed regularly along the irregular surface. The source and receiver spacings in horizontal direction are 12 m and 3 m, respectively. The source and receiver depth is 2 m. A Ricker wavelet with dominant frequency of 30 Hz is used as the source function to generate the observed data.

We first present the observed data and synthetic data calculated from the initial models with the source located at (0 m, 2 m) for comparison, as shown in Figure 2. SWs in the short profiles are much stronger than the BWs. Because the initial Q_α and Q_β models

are homogeneous without containing the strong attenuation anomalies at the near-surface, magnitudes of the synthetic data are stronger than those of the observed data, as indicated by the arrows in Figures 2a-2b and 2d-2e and the lines in Figures 2g-2h. In the numerical experiments, we design time windows to isolate the SWs and BWs, as indicated by the yellow and blue areas in Figures 2a-2b. SWs are used to invert for β and Q_β models and BWs are used to invert for α and Q_α models, respectively.

The sensitivity kernels are first calculated using different frameworks for comparison and analysis within the frequency band of [3 Hz, 25 Hz]. Figure 3 presents the Q_β and Q_α sensitivity kernels calculated using SWs and BWs with the true velocity models. The Q sensitivity kernels constructed in different frameworks are very similar and the attenuation anomalies at near-surface can be observed clearly. Figure 4 presents the β and Q_β sensitivity kernels calculated using SWs with the initial models. Figure 5 presents the α and Q_α sensitivity kernels calculated using BWs with the initial models. The velocity sensitivity kernels constructed by different frameworks are close, as shown in Figures 4a-4c and Figures 5a-5c. The Q_β sensitivity kernels calculated in framework-I and -III (Figures 4d and 4f) are close to the Q_β sensitivity kernels calculated using true velocity models (Figures 3a and 3c). However, some trade-off artifacts appear in the Q_β sensitivity kernel calculated in framework-II, as indicated by the arrows in Figure 4e. Structures of the Q_β anomalies at near-surface are not resolved clearly. In the Q_α sensitivity kernels calculated in framework-I and -III (Figures 5d and 5f), structures of the Q_α anomalies at near-surface appear to be more clear than those in the Q_α sensitivity kernels calculated using the true velocity models. This is caused by that the errors of low velocity zones are mapped into the Q_α sensitivity kernels, which enhanced the updates for Q_α anomalies. However, the Q_α sensitivity kernel calculated in framework-II appear to be distorted by stronger trade-off artifacts, as indicated by the arrow in Figure 5e.

Synthetic inversion experiments are next carried out for comparison. We first invert for the Q models using SWs and BWs with the true velocity models. The inverted Q models are presented in Figure 6. The well logs extracted from the inverted models at horizontal distance of 325 m are illustrated in Figures 8a and 8b. Figures 9a and 9b show the reductions of the normalized data misfits when using SWs and BWs, respectively. As can be seen that in the inverted Q models, the Q anomalies at near-surface can be reliably resolved, even though some artifacts appear in the deeper parts of the inverted Q_α models. The three different frameworks can provide comparable quality Q models with the true velocity models. I then invert for the Q models using SWs and BWs with the initial velocity models. The inversion results are given in Figure 7. The well logs of the inverted models are illustrated in Figures 8c and 8d. Figures 9c and 9d show the reductions of the normalized data misfits when using SWs and BWs. The attenuation anomalies at near-surface in the inverted Q_β models by framework-I and -III are clearly discernable, as indicated by the arrows in Figures 7a and 7c. However, the attenuation anomalies in the inverted Q_β model by framework-II are weaker and suffer from stronger trade-offs artifacts, as indicated by the arrow in Figure 7b. The inverted Q_α models with the initial velocity models are significantly damaged by the trade-off artifacts in the deeper parts. Structures of the Q_α anomalies at near-surface by framework-I and -III are better resolved than those obtained by framework-II, as indicated by the arrows in Figures 7d-7f. These observations suggest that in the presence of velocity errors, the Q sensitivity kernels calculated with memory

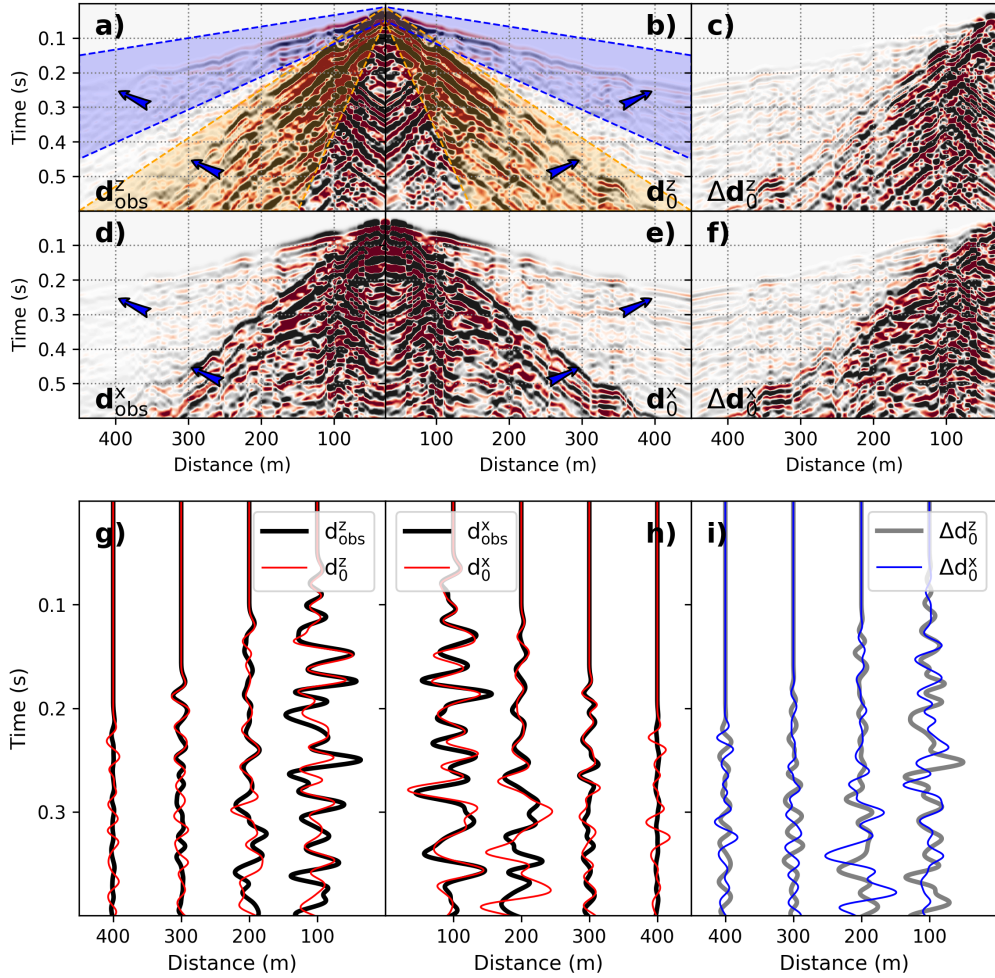


FIG. 2. (a-b) are the observed z component data ($\mathbf{d}_{\text{obs}}^z$) and synthetic z component data (\mathbf{d}_0^z) calculated from the initial models; (c) is the z component data residual ($\Delta \mathbf{d}_0^z$); (d-e) are the corresponding observed and synthetic x component data ($\mathbf{d}_{\text{obs}}^x$ and \mathbf{d}_0^x); (f) is the x component data residual ($\Delta \mathbf{d}_0^x$); (g) shows the comparison of the traces extracted in the observed (black) and synthetic (red) z component data; (h) shows the comparison of the traces extracted in the observed (black) and synthetic (red) x component data; (i) shows the z (gray) and x (blue) component data residual traces. This figure is adapted from Figure 11 in Pan et al. (2020).

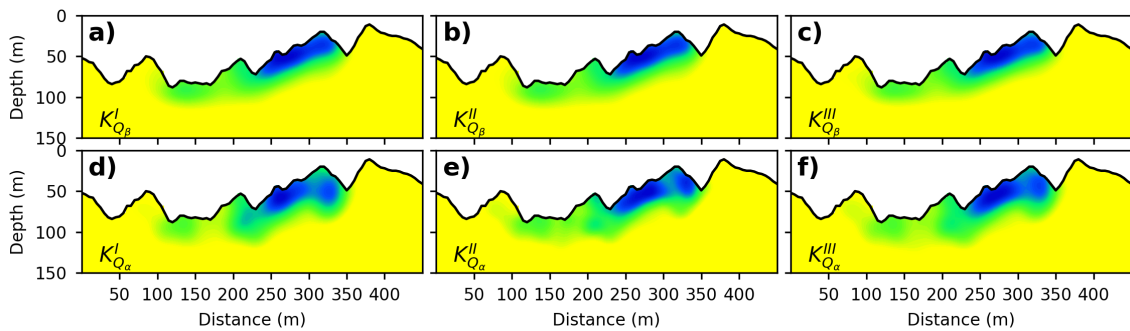


FIG. 3. (a-c) are the Q_β sensitivity kernels ($K_{Q_\beta}^I$, $K_{Q_\beta}^{II}$ and $K_{Q_\beta}^{III}$) calculated using SWs with true velocity models in framework-I, -II and -III; (d-e) are the Q_α sensitivity kernels ($K_{Q_\alpha}^I$, $K_{Q_\alpha}^{II}$ and $K_{Q_\alpha}^{III}$) calculated using BWs with true velocity models in different frameworks.

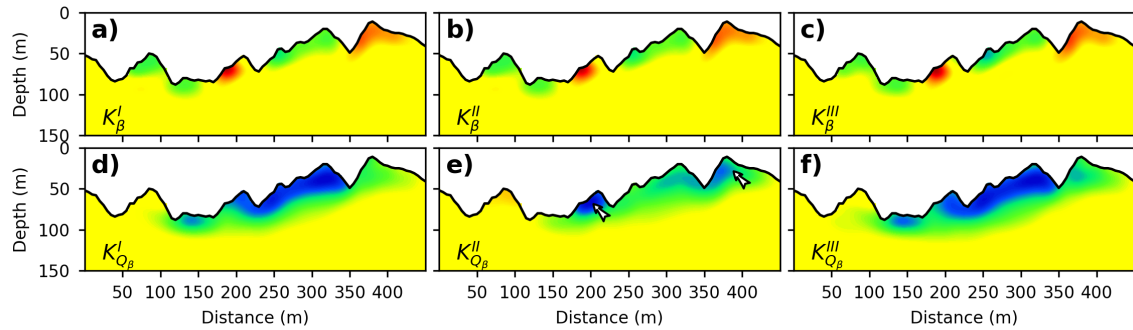


FIG. 4. (a-c) are the β sensitivity kernels (K_{β}^I , K_{β}^{II} and K_{β}^{III}) calculated using SWs in framework-I, -II and -III, respectively; (d-f) are the corresponding Q_{β} sensitivity kernels ($K_{Q_{\beta}}^I$, $K_{Q_{\beta}}^{II}$ and $K_{Q_{\beta}}^{III}$) calculated using SWs by different frameworks.

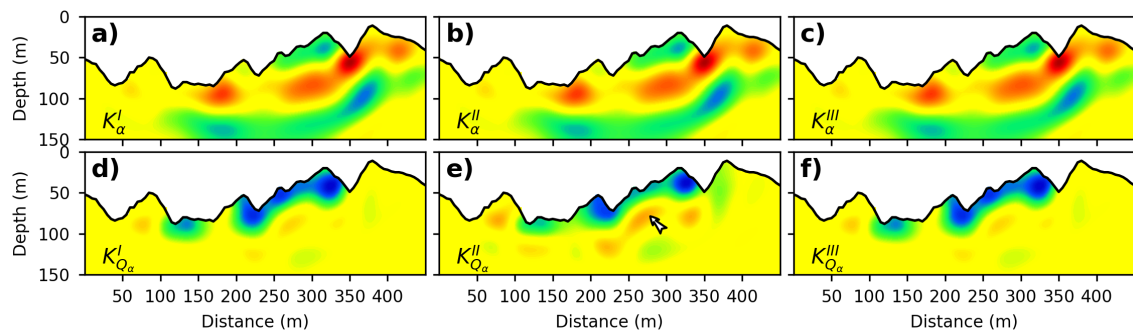


FIG. 5. (a-c) are the α sensitivity kernels (K_{α}^I , K_{α}^{II} and K_{α}^{III}) calculated using BWs in framework-I, -II and -III, respectively; (d-f) are the corresponding Q_{α} sensitivity kernels ($K_{Q_{\alpha}}^I$, $K_{Q_{\alpha}}^{II}$ and $K_{Q_{\alpha}}^{III}$) calculated using BWs by different frameworks.

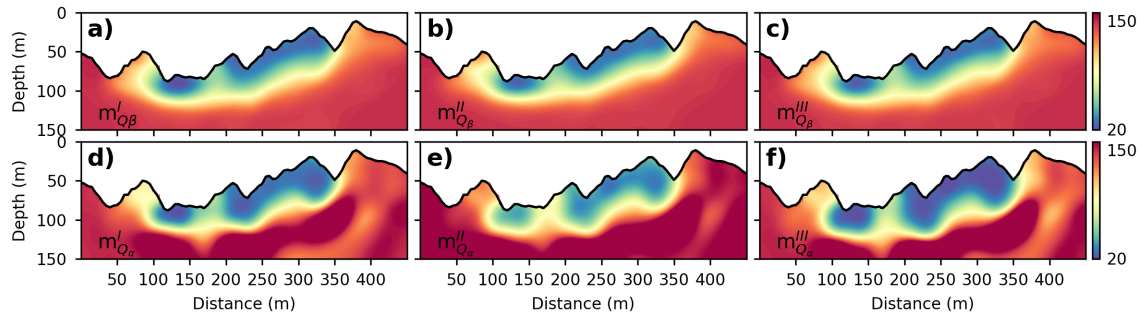


FIG. 6. (a-c) are the inverted Q_β models with the true velocity models using SWs in framework-I, -II and -III, respectively; (d-f) are the inverted Q_α models with the true velocity models using BWs in different frameworks.

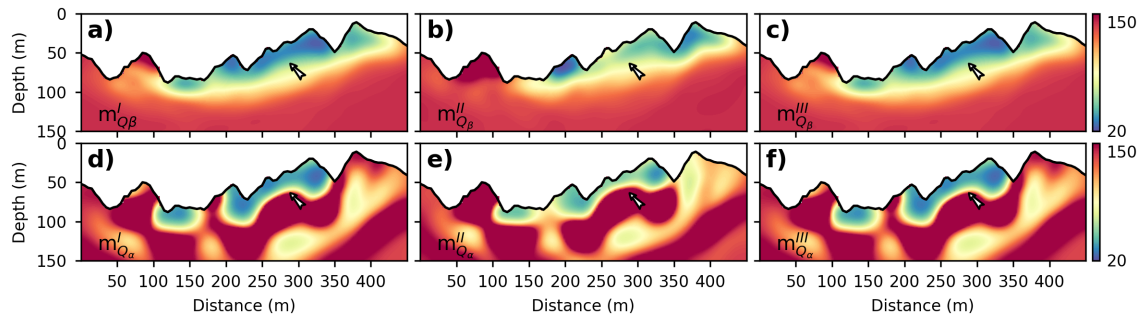


FIG. 7. (a-c) are the inverted Q_β models with the initial velocity models using SWs in framework-I, -II and -III, respectively; (d-f) are the inverted Q_α models with the initial velocity models using BWs in different frameworks.

variables in framework-I and -III are more accurate suffering from fewer trade-off artifacts.

We then carry out inversion experiments for simultaneously estimating the velocity and Q models. In stage-I, SWs are used to invert for β and Q_β models. The inverted models are presented in Figure 10. In stage-II, BWs are used to invert for α and Q_α models. The inverted models are presented in Figure 11. Well logs are extracted from the inversion results for comparison, as shown in Figure 12. Figures 13a and 13b show the reductions of the normalized data misfits by inversion of SWs and BWs in stage-I and -II, respectively. Framework-II suffers from slower convergence rate because of the trade-off artifacts in the Q sensitivity kernels. As iteration proceeds, the velocity models are gradually improved and the trade-off artifacts in the inverted Q models are suppressed. The final inversion results of framework-II are comparable to those obtained by framework-I and -III. However, because different adjoint sources are needed to calculate the velocity and Q sensitivity kernels, framework-II is almost two times more expensive than framework-I and -III. Finally, the synthetic data calculated from the inverted velocity and Q models in framework-III are illustrated in comparison with the observed data, as shown in Figure 14. The synthetic data match with the observed data closely and the corresponding data residuals also reduce significantly.

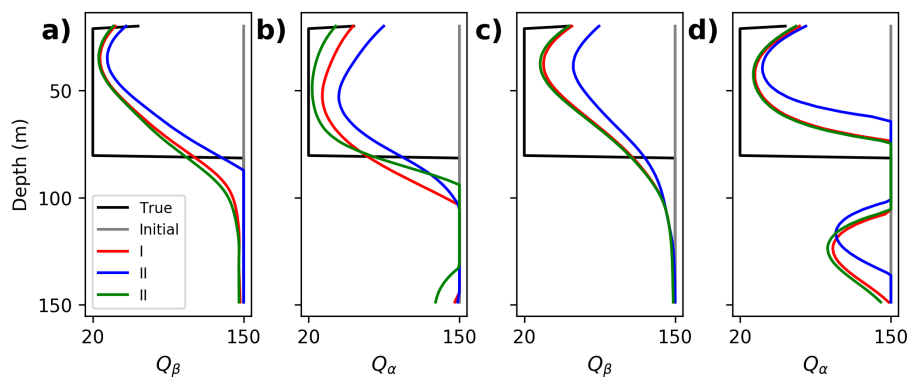


FIG. 8. (a) and (b) show the comparisons of well logs extracted from the inverted Q_β and Q_α models with the true velocity models at horizontal distance of 325 m in different frameworks; (c) and (d) show the comparisons of well logs extracted from the inverted Q_β and Q_α models with the initial velocity models in different frameworks. The black and gray lines indicate the true and initial models. The red, blue and green lines indicate the inverted models obtained by framework-I, -II and -III, respectively.

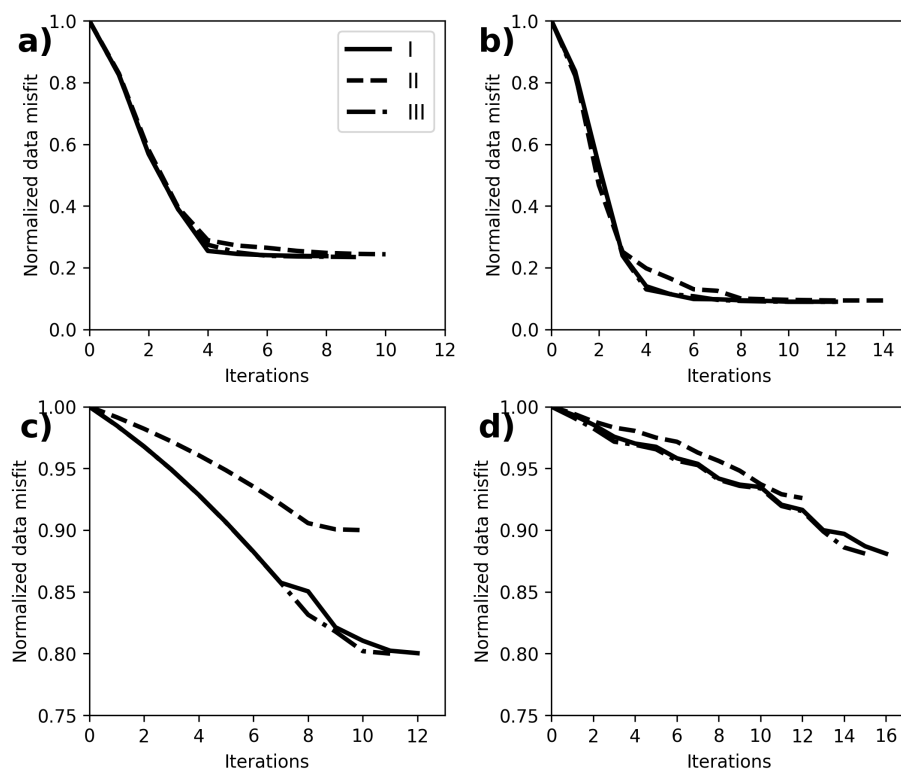


FIG. 9. (a) and (b) show the normalized data misfits reductions for Q_β and Q_α inversion using SWs and BWs with the true velocity models; (c) and (d) show the normalized data misfits reductions for Q_β and Q_α inversion using SWs and BWs with the initial velocity models.

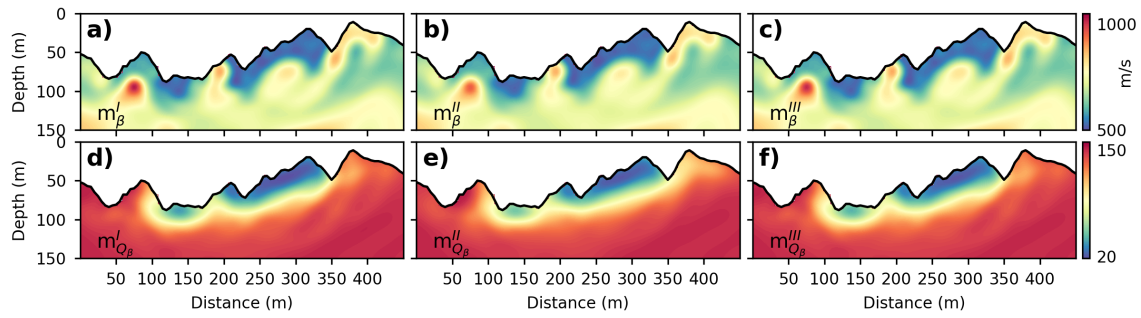


FIG. 10. (a-c) are the inverted β models (\mathbf{m}_{β}^I , \mathbf{m}_{β}^{II} and \mathbf{m}_{β}^{III}) using SWs in stage-I by framework-I, -II and -III, respectively; (d-f) are the inverted Q_{β} models ($\mathbf{m}_{Q_{\beta}}^I$, $\mathbf{m}_{Q_{\beta}}^{II}$ and $\mathbf{m}_{Q_{\beta}}^{III}$) using SWs in stage-I by different frameworks.

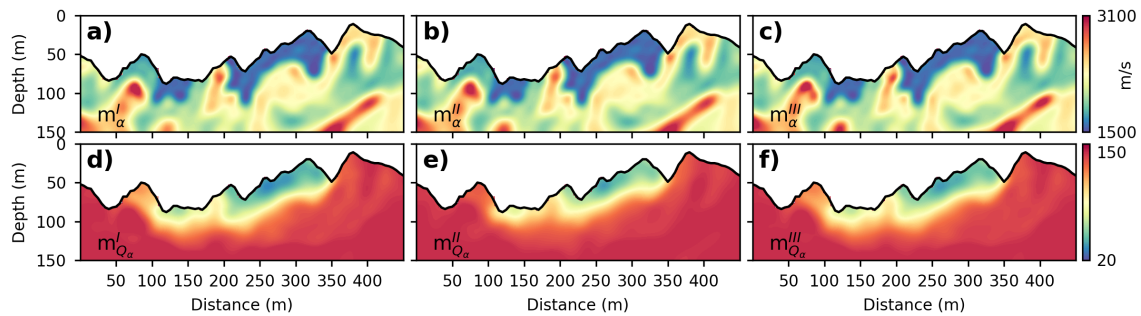


FIG. 11. (a-c) are the inverted α models (\mathbf{m}_{α}^I , \mathbf{m}_{α}^{II} and $\mathbf{m}_{\alpha}^{III}$) using SWs in stage-II by framework-I, -II and -III, respectively; (d-f) are the inverted Q_{α} models ($\mathbf{m}_{Q_{\alpha}}^I$, $\mathbf{m}_{Q_{\alpha}}^{II}$ and $\mathbf{m}_{Q_{\alpha}}^{III}$) using SWs in stage-II by different frameworks.

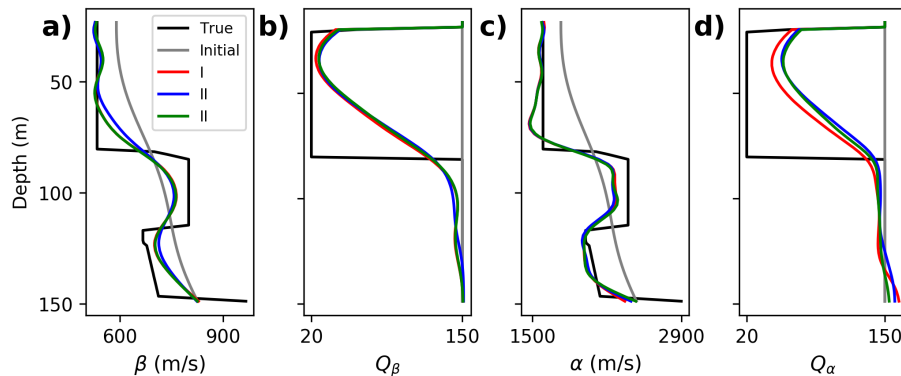


FIG. 12. (a-b) show comparisons of well logs of the inverted β and Q_{β} models by inversion of SWs in different frameworks; (c-d) show comparisons of well logs of the inverted α and Q_{α} models by inversion of BWs in different frameworks. The black and gray lines indicate the true and initial models. The red, blue and green lines indicate the inverted models obtained by framework-I, -II and -III.

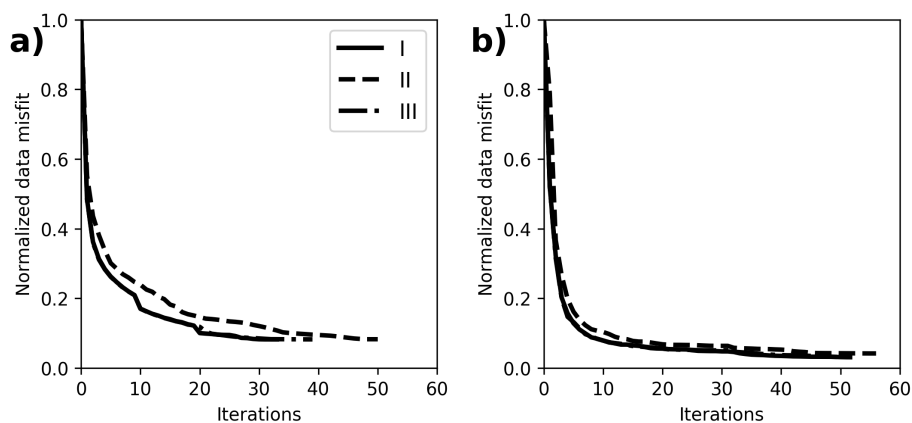


FIG. 13. (a) shows the normalized data misfits reductions by inversion of SWs in stage-I; (b) shows the normalized data misfits reductions by inversion of BWs in stage-II. The solid, dashed, and dash-dotted lines indicate framework-I, -II and -III, respectively.

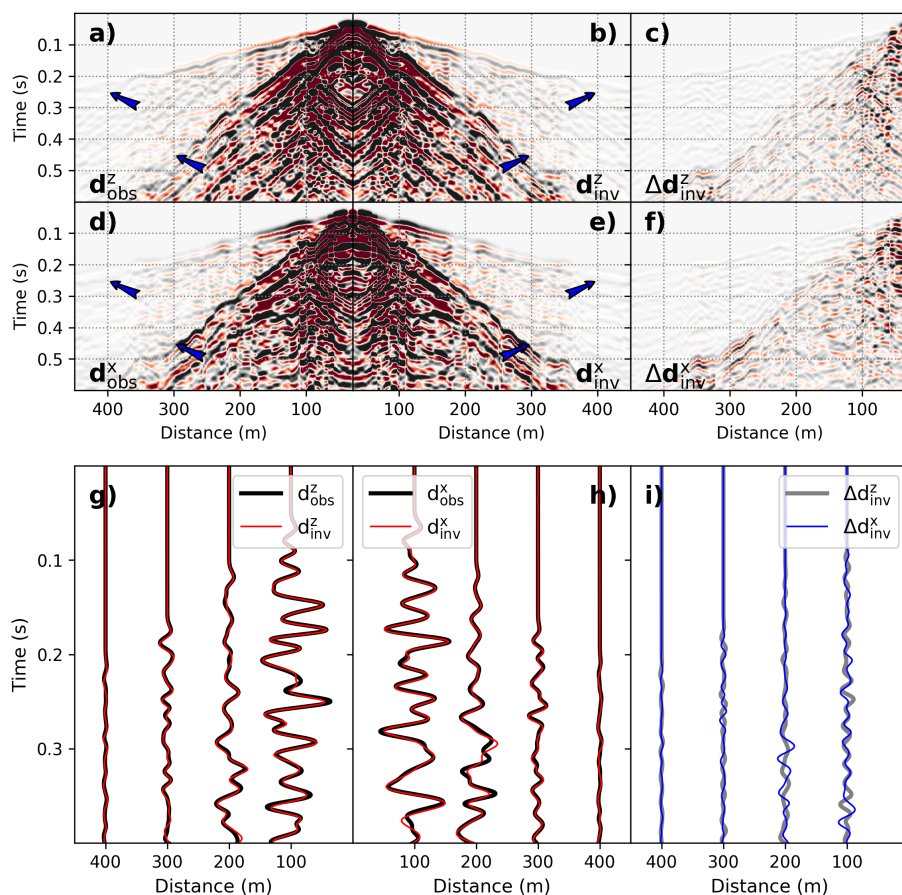


FIG. 14. (a-b) show the observed z component data ($\mathbf{d}_{\text{obs}}^z$) and synthetic z component data ($\mathbf{d}_{\text{inv}}^z$) calculated from the inverted models; (c) shows the z component data residuals ($\Delta \mathbf{d}_{\text{inv}}^z$); (d-e) show the corresponding observed and synthetic x component data ($\mathbf{d}_{\text{obs}}^x$ and $\mathbf{d}_{\text{inv}}^x$); (f) shows the x component data residuals ($\Delta \mathbf{d}_{\text{inv}}^x$); (g) shows the comparison of the traces extracted in the observed (black) and synthetic (red) z component data; (h) shows the comparison of the traces extracted in the observed (black) and synthetic (red) x component data; (i) shows the z (gray) and x (blue) component data residual traces.

DISCUSSIONS

This study investigates the theories of three different frameworks for time domain viscoelastic FWI based on the GSLS model. Inaccuracy of the Q sensitivity kernels in framework-II arises from the inconsistency between the physical models in forward modelling and sensitivity kernel derivation.

Because envelope measures the instantaneous amplitude of the seismic signals, the ED misfit function helps reduce the trade-off artifacts caused by velocity errors for Q inversion. However, this advantage of the ED misfit function relies significantly on high quality of the seismic data. In practical seismic data, many other factors including source mechanism, geometrical spreading, etc, can produce influences on seismic amplitudes. Thus, the field seismic data should be pre-processed carefully to preserve the amplitudes. Furthermore, it is necessary to examine the Q sensitivity kernels calculated other misfit functions including central frequency, spectral-ratio, etc.

CONCLUSIONS

In this research, we revisit the theories of three different frameworks for constructing the sensitivity kernels for time domain viscoelastic FWI based on the GSLS model. In framework-I and -III, the Q sensitivity kernels are constructed with memory variables, whereas in framework-II, the Q sensitivity kernels are constructed by introducing additional adjoint source. In the numerical experiments, synthetic examples are given to examine the velocity and Q sensitivity kernels in different frameworks. The observations suggest that the Q sensitivity kernels constructed with memory variables in framework-I and -III are more accurate suffering from fewer trade-off artifacts in the presence of velocity errors. When simultaneously estimating the velocity and Q models, these different frameworks can provide comparable quality inversion results. However, framework-II converges more slowly and is two times more expensive than framework-I and -III.

REFERENCES

- Blanch, J. O., Robertsson, J. O. A., and Symes, W. W., 1995, Modeling of a constant Q : Methodology and algorithm for an efficient and optimally inexpensive viscoelastic technique: *Geophysics*, **60**, No. 1, 176–184.
- Bohlen, T., 2002, Parallel 3-D viscoelastic finite difference seismic modelling: *Computer & Geosciences*, **28**, 845–870.
- Brossier, R., 2011, Two-dimensional frequency-domain visco-elastic full waveform inversion: Parallel algorithms, optimization and performance: *Computer & Geosciences*, **37**, 444–445.
- Charara, M., Barnes, C., and Tarantola, A., 2000, Full waveform inversion of seismic data for a viscoelastic medium, in *Methods and Applications of Inversion*: Springer.
- Fichtner, A., and van Driel, M., 2014, Models and Fréchet kernels for frequency-(in)dependent Q : *Geophysical Journal International*, **198**, 1878–1889.
- Futterman, W. I., 1962, Dispersive body waves: *Journal of Geophysical Research*, **67**, 5279–5291.
- Innanen, K. A., 2011, Inversion of the seismic AVF/AVA signatures of highly attenuative targets: *Geophysics*, **76**, No. 1, R1–R14.
- Innanen, K. A., 2014, Seismic AVO and the inverse Hessian in precritical reflection full waveform inversion: *Geophysical Journal International*, **199**, 717–734.

- Keating, S., and Innanen, K. A., 2019, Parameter cross-talk and modeling errors in viscoacoustic seismic full-waveform inversion: *Geophysics*, **84**, No. 4, R641–R653.
- Kolsky, H., 1952, The propagation of stress pulses in viscoelastic solids: *Philosophical Magazine*, **1**, 693–710.
- Komatitsch, D., and Tromp, J., 2005, Introduction to the spectral-element method for 3-D seismic wave propagation: *Geophysical Journal International*, **139**, 806–822.
- Liu, H., Anderson, D. L., and Kanamori, H., 1976, Velocity dispersion due to anelasticity; implications for seismology and mantle composition: *Geophys. J. R. Astron. Soc.*, **47**, No. 1, 41–58.
- Liu, Q., and Tromp, J., 2006, Finite-Frequency Kernels Based on Adjoint Methods: *Bulletin of Seismological Society of America*, **96**, No. 6, 2383–2397.
- Liu, Q., and Tromp, J., 2008, Finite-frequency sensitivity kernels for global seismic wave propagation based upon adjoint methods: *Geophysical Journal International*, **174**, 265–286.
- Operto, S., Gholami, Y., Prieux, V., Ribodetti, A., Brossier, R., Métivier, L., and Virieux, J., 2013, A guided tour of multiparameter full waveform inversion with multicomponent data: from theory to practice: *The Leading Edge*, **32**, 1040–1054.
- Pan, W., and Innanen, K. A., 2019, Amplitude-based misfit functions in viscoelastic full-waveform inversion applied to walk-away vertical seismic profile data: *Geophysics*, **84**, No. 5, B335–B351.
- Pan, W., Innanen, K. A., and Wang, Y., 2020, SeisElastic2D: An open-source package for multiparameter full-waveform inversion in isotropic-, anisotropic- and visco-elastic media: *Computers & Geosciences*, **145**, 104,586.
- Pratt, G. R., Shin, C., and Hicks, G. J., 1998, Gauss-Newton and full Newton methods in frequency-space seismic waveform inversion: *Geophysical Journal International*, **133**, 341–362.
- Robertsson, J. O., Blanch, J. O. A., and Symes, W. W., 1994, Viscoelastic finite-difference modeling: *Geophysics*, **59**, 1444–1456.
- Tarantola, A., 1984, Inversion of seismic reflection data in the acoustic approximation: *Geophysics*, **49**, 1259–1266.
- Tromp, J., Tape, C., and Liu, Q., 2005, Seismic tomography, adjoint methods, time reversal, and banana-doughnut kernels: *Geophysical Journal International*, **160**, 195–216.
- Virieux, A., and Operto, S., 2009, An overview of full-waveform inversion in exploration geophysics: *Geophysics*, **74**, No. 6, WCC1–WCC26.